Cluster formation in relativistic nucleus-nucleus collisions

T. Ogawa,* T. Sato, and S. Hashimoto
Research Group for Radiation Transport Analysis, Japan Atomic Energy Agency, Tokai, Ibaraki, Japan

K. Niita
Research Organization for Information Science and Technology, Tokai, Ibaraki, Japan

(Received 20 February 2018; revised manuscript received 6 June 2018; published 13 August 2018)

An event generator for exclusive simulation of nucleus-nucleus collisions based on quantum molecular dynamics is developed. A comparison of the results obtained using this event generator with earlier measurements show that the yields of pions, kaons, antiprotons, deuterons, and nuclear fragments in the collisions of various nuclei pair such as Si-Al and Pb-Pb in the energy range of a few to 100 A GeV are predicted successfully. The Lorentz-covariant description of nucleon-nucleon interactions plays a critical role in reproducing fragment yields in peripheral collisions. Secondary meson yields from nucleus-nucleus collisions are well reproduced by incorporating the production and decay of resonances of up to 2 GeV/c^2 and strings. This model can therefore be used for analysis and planning of high-energy particle physics experiments, prediction of cosmic ray transport, and shielding design of high-energy heavy-ion accelerators.

DOI: 10.1103/PhysRevC.98.024611

I. INTRODUCTION

Information about nucleus-nucleus collisions is important for investigating issues in fundamental physics such as parameters of the nuclear equation of state [1], phase transition of nuclear matter [2], and properties of exotic nuclei [3]. Heavy-ion collision experiments at facilities such as LHC-ALICE (Large Hadron Collider—A Large Ion Collider Experiment) and RHIC (Relativistic Heavy Ion Collider) are performed to obtain experimental evidence to support the findings of theoretical studies. Moreover, in cosmic-ray physics, information about nucleus-nucleus collisions is important for predicting the interaction of heavy ions in galactic cosmic rays and the atmosphere. Prediction of the secondary particle production and fragment yield is crucial for cosmic-ray detectors such as the Fermi-LAT [4] and the Telescope Array [5]. It is suggested that γ-ray detector satellites capture the prompt γ rays produced by cosmic-ray heavy ions fragmented in the atmosphere in addition to those that come directly from astronomical objects. Prediction of the former is necessary for background subtraction. In the case of Telescope Array detectors, which are placed on Earth, reconstruction of particle trajectories is fundamental for identification of incident cosmic rays. Particle trajectories are reconstructed based on the detected signals and reaction simulation. Microscopic reaction models to simulate nucleus-nucleus collisions, which are used in such studies, were developed based on a few theories. The most popular methods are the time-dependent Hartree-Fock method [6–13], quantum molecular dynamics (QMD) model [14–23], cascade models [24–28], Boltzmann-Uehling-Uhlenbeck (BUU) model [29–36], and jet + string models [37–39].

In nucleus-nucleus collision experiments, the observed events are filtered based on the multiplicities of specific secondary particles or isotopic identities of residual nuclei. Therefore, exclusive reproduction of each event considering resonances, string decays, interaction between particles, and clusterization of nucleons in the final stage is necessary for performing simulation of the experiments. In earlier studies, production of baryons and mesons in nucleus-nucleus collisions was well reproduced as a combination of incoherent binary collisions [24]. However, to simulate the production of residual nuclei, treatment of interactions inside the spectator part of nuclei is necessary.

One of the most common approaches to nucleus-nucleus collision simulation, QMD [14] explicitly calculates the interaction of every single particle in the system; such a simulation can therefore be used to calculate particle multiplicities and fragment yields in each reaction explicitly. TuQMD [40], ImQMD [41], RQMD [42], UrQMD [22], and JQMD [23] were developed to simulate nucleus-nucleus reactions. These codes have been used to successfully reproduce secondary particle yields. However, in these codes, nuclei were disintegrated spuriously or excited during time evolution, mainly owing to the nonrelativistic description of the Hamiltonian. The nonrelativistic equation of motion can be derived easily from the nonrelativistic Hamiltonian, which is written as

$$H = \sum_i \sqrt{\mathbf{p_i}^2 + m_i^2} + V, \tag{1}$$

where $\mathbf{p_i}$ is the momentum of the ith particle, m_i is the mass of the ith particle, and V is the system potential. By contrast, the relativistic Hamiltonian is written as

$$H = \sum_i \sqrt{\mathbf{p_i}^2 + m_i^2 + 2m_i V_i}, \tag{2}$$

*ogawa.tatsuhiko@jaea.go.jp

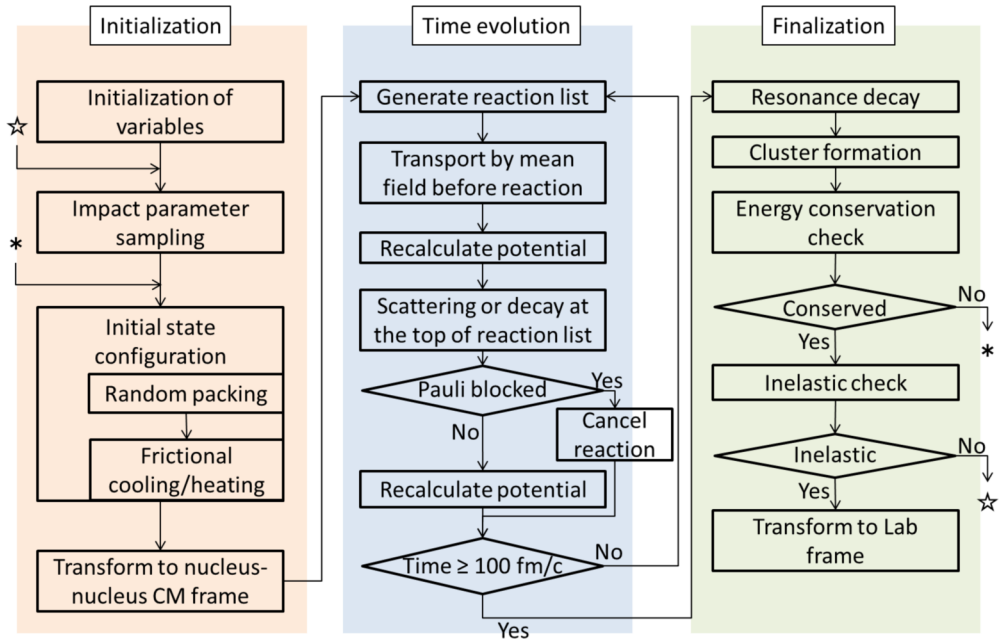

FIG. 1. Flowchart of the JAMQMD algorithm.

where V_i is the potential of the ith particle. In this case, the particle mass is no longer a constant but is effectively written as $\sqrt{m_i^2 + 2m_i V_i}$; therefore, the equation of motion cannot be obtained without additional assumptions. In a few codes, instead of solving the relativistic equation of motion, spurious excitation or decay was suppressed by introducing Pauli force and freezing the nucleons until impact. Alternatively, the impact parameter was intentionally limited and both peripheral collisions and spurious reactions were disregarded. These treatments resulted in nonconservation of energy, an incorrect specific heat of the nucleus, or inaccurate simulation of peripheral collisions, leading to undesirable effects on the formation of residual nuclei. Antisymmetrized molecular dynamics (AMD) and Fermionic molecular dynamics (FMD) are advantageous in the sense that they can start from the rigorous ground-state configuration [43,44], but asymmetrization is unrealistically CPU-expensive for analysis of heavy-nucleus collisions (such as Pb-Pb collisions). Moreover, AMD and FMD tend to underestimate secondary particles owing to the rigorously cramped ground-state configuration. Coalescence models [45,46] are often used to simulate cluster formation; however, they cannot be applied to the formation of heavy residues. Hence, the QMD, AMD, and FMD models are useful for simulating either nuclear structures or particle yields, and residual nucleus production remains an issue.

Mancusi *et al.* [47] showed that the relativistic equation of motion for QMD calculation can be derived by their prescription. Low-energy ($\leqslant 3A$ GeV) heavy-ion reaction model JQMD version 2.0 [48] was developed based on their prescription. Meanwhile, Nara *et al.* developed a cascade-type hadronic collision event generator (JAM [24]) based on the reasonable cross-section parametrization of high-energy baryons and mesons. The idea of the present study is to incorporate these two elements into a QMD model to develop a reaction model (hereafter referred to as JAMQMD) that can reasonably simulate particle production and fragment yield in high-energy nucleus-nucleus reactions of up to 1 ATeV of incident energy. In JAMQMD, artificial corrections such as freezing of nuclei and coalescence on the nuclear surface are not necessary because nuclei are formed and sustained by the interaction between nucleons. Meanwhile, the calculation scheme is based fundamentally on QMD; therefore, the calculation is as fast as conventional QMD models, unlike the AMD-type models.

The calculation performed using JAMQMD was compared with the data on earlier measurements in the energy range of a few A GeV (resonance dominant) to 100 A GeV (string dominant) to verify its performance. The comparison shows that JAMQMD can reproduce not only the particle production but also the yields of light clusters and heavy residues. Moreover, it is shown that accurate reproduction of the heavy-fragment yield requires a relativistic equation of motion. In Sec. II, we give a description of the calculation procedure (Sec. II A, Configuration of the Initial State of Interacting Nuclei; Sec. II B, Time Evolution of Nuclei Based on Intranucleon Interaction; Sec. II C, Determination of the Final State), formula, and parameters of JAMQMD. In Sec. III A, the stability of the nuclei initialized in Sec. II A was tested. In Secs. III B and III C, we compare the fragment yield distribution and particle yields calculated by JAMQMD with the corresponding experimental data. Finally, we give a summary and outlook in Sec. IV.

II. MODEL

An outline of the developed model, JAMQMD, is shown in Fig. 1. JAMQMD consists of three phases: initialization, time evolution, and finalization. When the simulation proceeded to the next phase, the frame of particles was transferred. Initialization, time evolution, and finalization were calculated

in the nuclear-rest, nucleus-nucleus center-of-mass (CM), and laboratory frames, respectively.

A. Initialization

The initial state of the nucleus (i.e., arrangement of nucleons in the phase space) was configured using the random packing method associated with frictional cooling and heating, which adjusts the excitation energy of the nucleus. Random packing was carried out using the following scheme. The nuclear radius (r) and diffuseness (a) were assumed to be

$$r = 1.124 \times A^{1/3}, \tag{3}$$

$$a = 0.2, \tag{4}$$

where A is the mass number of the nucleus. The spatial coordinates of the nucleons were sampled randomly based on the Woods-Saxon distribution defined by the above radius and diffuseness while keeping the nucleon-nucleon distance larger than 1.0 fm (isospin asymmetric pairs) or 1.5 fm (isospin symmetric pairs). If the sampled coordinate did not satisfy this condition, the coordinate was rotated randomly (i.e., angular coordinates were changed randomly without changing the distance from the center). The momenta of the nucleons were sampled randomly below the local Fermi momentum calculated as

$$p_{\rm f} = \hbar c \left(\frac{3\pi^2\rho}{2}\right)^{1/3}, \quad \sqrt{p_{\rm x-r}^2 + p_{\rm y-r}^2 + p_{\rm z-r}^2} \leqslant p_{\rm f}, \tag{5}$$

where $p_{\rm x-r}$, $p_{\rm y-r}$, and $p_{\rm z-r}$ are the x, y, and z components of the momentum in the nucleus-rest frame and ρ is the local nucleon density.

Thus far, nuclei have been configured in their rest frame. The configured ground-state nuclei were transferred from the rest frame to the nucleus-nucleus CM frame. To save CPU time, the colliding nuclei were placed with 4 fm ($E_L ab \leqslant 10$ A GeV) or 2 fm ($E_L ab \geqslant 10$ A GeV) of longitudinal distance between surfaces. In addition, by shifting the momenta and spatial coordinates, the Coulomb repulsion between colliding nuclei (Rutherford scattering) was considered. Thus the nuclei were transformed to the CM frame. The nuclei are located close to each other such that they almost touch by the coordinate transform.

B. Time evolution

In our model, elastic and inelastic reactions between close hadron pairs are treated as binary instant collisions, whereas long-range interaction is described as the mean field, which changes the momentum of particles gradually. In the nonrelativistic limit, the equation of motion is written as

$$\dot{\mathbf{r}}_\mathbf{i} = \frac{\mathbf{p_i}}{m_i} + \frac{\partial\langle\hat{V}\rangle}{\partial\mathbf{p_i}}, \quad \dot{\mathbf{p}}_\mathbf{i} = -\frac{\partial\langle\hat{V}\rangle}{\partial\mathbf{r_i}}, \tag{6}$$

where $\langle\hat{V}\rangle$ is the system potential, $\mathbf{r_i}$ is the spatial coordinate of the centroid of the ith particle, $\mathbf{p_i}$ is the momentum of the ith particle, and m_i is the mass of the ith particle. The following conditions were introduced to describe the equation of motion in a Lorentz-covariant manner [47]:

(i) define the distance between nucleons as the Lorentz-covariant scalar using the four-momentum,
(ii) define a Hamiltonian composed of $8N$ variables ($4N$ positional coordinates + $4N$ momentum coordinates), and
(iii) eliminate $2N$ degrees of freedom by applying the on-mass-shell condition and adopting the common time coordinate,

where N is the number of particles in the system. The common time coordinate is an approximation but this is critical to solving the equation of motion. The adequacy of this approximation is illustrated in Sec. III A. Under these conditions, the equation of motion is written as Eq. (7),

$$\begin{aligned}
\dot{\mathbf{r}}_\mathbf{i} &= \frac{\mathbf{p_i}}{p_i^0} + \sum_j^N \frac{m_j}{p_j^0}\frac{\partial\langle\hat{V}_j\rangle}{\partial\mathbf{p_i}}, \\
\dot{\mathbf{p}}_\mathbf{i} &= -\sum_j^N \frac{m}{p_j^0}\frac{\partial\langle\hat{V}_j\rangle}{\partial\mathbf{r_i}}, \\
p_i^0 &= \sqrt{\mathbf{p_i}^2 + m_i^2 + 2m_i\langle\hat{V}_i\rangle},
\end{aligned} \tag{7}$$

where $\langle\hat{V}_j\rangle$ is the potential of the jth particle. The potential, which consists of the Skyrme term, symmetry term, and Coulomb term [23], is written as

$$\begin{aligned}
V_i = {} & \frac{1}{2}\frac{A}{\rho_{\rm s}}\langle\rho_i\rangle + \frac{1}{1+\tau}\frac{B}{\rho_{\rm s}^\tau}\langle\rho_i\rangle^\tau + \frac{1}{2}\sum_j \frac{c_i c_j\, e^2}{|\mathbf{r_i} - \mathbf{r_j}|} \\
& \times {\rm erf}\left(\frac{|\mathbf{r_i} - \mathbf{r_j}|}{\sqrt{4L}}\right) + \frac{C_{\rm s}}{2\rho_{\rm s}}\sum_j (1 - 2|c_i - c_j|)\rho_{ij},
\end{aligned} \tag{8}$$

where A is a Skyrme force parameter (=−219.4 MeV), $\rho_{\rm s}$ is the saturation density (=0.168 fm^{-3}), $\langle\rho_i\rangle$ is the overlap integral of wave packets between the ith nucleon and all the other nucleons, B is another Skyrme force parameter (=165.3 MeV), τ is 4/3, c_i is 1 for protons and 0 for neutrons, e is the elementary charge, $\mathbf{r_i}$ denotes the spatial coordinates of the ith particle, L is the width of the wave packet representing nucleons (=2 fm^2), $C_{\rm s}$ is the symmetry energy parameter (=25 MeV), and ρ_{ij} is the overlap integral of the wave functions of the ith and jth nucleons. The wave packet of nucleons was assumed as Gaussian with 2 fm^2 of width to calculate the overlap integral. The first two, third, and fourth terms are Skyrme-type force terms, the Coulomb force term, and the symmetry term, respectively. The Lorentz-covariant description of motion, written as Eq. (8) [47], and the interaction between nucleons, written as Eq. (8), can keep the nuclei stable not only in the nucleus rest frame but also in the CM frame of the colliding nuclei.

Particles transport was tracked for 0.5 fm/c of time step by default. But if the next collision was expected during the next 0.5 fm/c of time step, the particles were transported until the next collision occurred. In some codes, particle motion is tracked at fixed time intervals (e.g., 1 fm/c), and the particle pairs colliding in the time step are determined at the end of every interval. However, central high-energy collisions can result in dense nuclear matter, in which one particle collides

TABLE I. Reaction channels considered in JAMQMD.

$p + p \to p + \Delta^+$	$n + n \to n + \Delta^0$	$n + p \to n + \Delta^+$
$p + p \to n + \Delta^{++}$	$n + n \to p + \Delta^-$	$n + p \to p + \Delta^0$
$p + p \to p + p^*$	$n + n \to n + n^*$	$n + p \to n + p^*$
$p + p \to \Delta^+ + \Delta^+$	$n + n \to \Delta^0 + \Delta^0$	$n + p \to n^* + p$
$p + p \to \Delta^0 + \Delta^+ +$	$n + n \to \Delta^+ + \Delta^-$	$n + p \to \Delta^0 + \Delta^+$
		$n + p \to \Delta^- + \Delta^{++}$

with more than one particle in a fixed time step. To maintain the proper order of collisions, particles were tracked using a variable time interval. The collision timing was calculated in the nucleus-nucleus CM frame as the timing at which the colliding particles are the closest point. Owing to the relativity of simultaneity, the timing of one particle did not agree with that of the other. Therefore the collision timing was defined as the average of their times.

In the case of baryon-baryon cross sections, the total reaction cross sections consisted of

$$\sigma_{\mathrm{totBB}}(\sqrt{s}) = \sigma_{\mathrm{BW}}(\sqrt{s}) + \sigma_{\mathrm{el}}(\sqrt{s}) + \sigma_{\mathrm{s}}(\sqrt{s}), \tag{9}$$

where σ_{totBB} is the total cross section, $\sqrt{s}$ is the total CM energy, σ_{BW} is the resonance cross section expressed in the Breit-Wigner form, σ_{el} is the elastic cross section, and σ_{s} is the string formation cross section. The total reaction cross section was taken from the literature [49]. The elastic reaction cross sections were expressed based on the parametrization with correction for in-medium suppression [50]. The inelastic reaction cross section was calculated by subtracting the elastic reaction cross section from the total reaction cross section. When the inelastic reaction was sampled, resonance reaction cross sections were calculated using the method described below. All the resonance cross sections subtracted from the inelastic cross section leave the string production cross section. Inelastic resonance channels, listed in Table I, were considered. Resonance production cross sections were fitted using the function

$$\sigma_{\mathrm{R}}(\sqrt{s}) = \frac{a(\sqrt{s}/\sqrt{s_{\mathrm{th}}} - 1)^b d}{(\sqrt{s}/c - 1)^2 + d^2}, \tag{10}$$

where σ_{R} is the resonance cross section, $\sqrt{s_{\mathrm{th}}}$ is the reaction threshold, and a, b, c, and d are the fitting parameters. This fitting function and the fitting parameters were taken from [24]. As illustrated in Fig. 3 in [24], this fitting can reproduce various exclusive meson production cross sections with a good accuracy. A transition matrix is necessary to accurately determine the reaction channel to be realized; however, in JAMQMD, it was assumed that the transition probability is proportional to the integral of the transition strength over the spin, isospin, and product mass. Pionic fusion reactions and s-wave pion production reactions were not treated explicitly but included effectively in $\mathrm{N} + \mathrm{N} \to \mathrm{N} + \Delta$ reactions and $\mathrm{N} + \mathrm{N} \to \mathrm{N} + \mathrm{N}(1440)$ reactions, respectively. Therefore, the resonance reaction channels specified in Table I were considered, where Δ denotes all delta resonances from 1232 to 1950 MeV, and n^* and p^* denote all N* resonances from 1440 to 1990 MeV.

In the case of baryon-meson combination, cross sections were decomposed depending on the type of meson,

$$\sigma_{\mathrm{tot}\pi\mathrm{B}}(\sqrt{s}) = \sigma_{\mathrm{BW}}(\sqrt{s}) + \sigma_{\mathrm{el}}(\sqrt{s}) + \sigma_{\mathrm{s\text{-}S}}(\sqrt{s}) + \sigma_{\mathrm{t\text{-}S}}(\sqrt{s}), \tag{11}$$

$$\sigma_{\mathrm{tot}\bar{\mathrm{K}}\text{-}B}(\sqrt{s}) = \sigma_{\mathrm{BW}}(\sqrt{s}) + \sigma_{\mathrm{el}}(\sqrt{s}) + \sigma_{\mathrm{ch}}(\sqrt{s}) + \sigma_{\pi\mathrm{Y}}(\sqrt{s}) + \sigma_{\mathrm{s\text{-}S}}(\sqrt{s}) + \sigma_{\mathrm{t\text{-}S}}(\sqrt{s}), \tag{12}$$

$$\sigma_{\mathrm{totK\text{-}B}}(\sqrt{s}) = \sigma_{\mathrm{el}}(\sqrt{s}) + \sigma_{\mathrm{ch}}(\sqrt{s}) + \sigma_{\mathrm{t\text{-}R}}(\sqrt{s}) + \sigma_{\mathrm{t\text{-}S}}(\sqrt{s}), \tag{13}$$

where $\sigma_{\mathrm{tot}\pi\text{-}\mathrm{B}}$, $\sigma_{\mathrm{tot}\bar{\mathrm{K}}\text{-}\mathrm{B}}$, and $\sigma_{\mathrm{totK\text{-}B}}$ are the total cross sections of π-baryon, $\bar{K}$-baryon, and K-baryon combinations, respectively, σ_{BW} is the resonance cross section expressed in the Breit-Wigner form, σ_{el} is the elastic cross section, $\sigma_{\mathrm{s-S}}$ is the s-channel string formation cross section, $\sigma_{\mathrm{t-S}}$ is the t-channel string formation cross section, σ_{ch} is the charge exchange reaction cross section, $\sigma_{\pi\mathrm{Y}}$ is the hyperon (Λ, Σ) production cross section, and $\sigma_{\mathrm{t\text{-}R}}$ is the t-channel resonance production cross section.

In the case of meson-meson combination, cross sections were expressed using the combination

$$\sigma_{\mathrm{totMM}}(\sqrt{s}) = \sigma_{\mathrm{BW}}(\sqrt{s}) + \sigma_{\mathrm{el}}(\sqrt{s}) + \sigma_{\mathrm{t\text{-}R}}(\sqrt{s}) + \sigma_{\mathrm{s\text{-}S}}(\sqrt{s}) + \sigma_{\mathrm{t\text{-}S}}(\sqrt{s}). \tag{14}$$

where σ_{totMM} denotes the total meson-meson reaction cross section.

These cross sections were determined by fitting if experimental data were available; otherwise, the total and elastic reaction cross sections were calculated using the additive quark model [22,51,52]. The outgoing angular distribution of t-channel resonances was expressed as

$$\frac{d\sigma_{\mathrm{t-R}}}{dt} \propto \exp(bt),$$
$$b = 2.5 + 0.7\log(s/2)(\sqrt{s} \geqslant 2.17\ \mathrm{GeV}), \tag{15}$$

where t denotes the Mandelstam variable t. Below 2.17 GeV, the value of b was taken from [23].

The mass of resonances was sampled randomly from the relativistic Breit-Wigner distribution written as

$$A(m^2) = \frac{1}{\pi}\frac{m_{\mathrm{R}}\Gamma(m)}{\left(m^2 - m_{\mathrm{R}}^2\right)^2 + m_{\mathrm{R}}^2\Gamma(m)^2}, \tag{16}$$

where m_R is the resonance mass, and Γ is the total decay width calculated using Eq. (17),

$$\Gamma = \Sigma_{\mathrm{decay\ channel}}\Gamma_{\mathrm{ch}},$$
$$\Gamma_{\mathrm{ch}} = \Gamma_R^0\frac{m_R}{m}\left(\frac{p_{\mathrm{CM}}(m)}{p_{\mathrm{CM}}(m_R)}\right)^{2l+1}\frac{1.2}{1 + 0.2\left(\frac{p_{\mathrm{CM}}(m)}{p_{\mathrm{CM}}(m_R)}\right)^{2l+1}}, \tag{17}$$

where Γ_{ch} is the decay width of the decay channel, and l and p_{CM} are the relative angular momentum and relative momentum of the decay products in the decay channel, respectively. The inverse reaction cross sections were calculated based on the extended detailed balance [53]. The cross sections were

calculated as

$$\frac{d\sigma_{\rm inv}}{d\Omega} = \frac{(2S_1+1)(2S_2+1)}{(2S_3+1)(2S_4+1)}\frac{p_{12}^2}{p_{34}^2}\frac{d\sigma}{d\Omega}, \tag{18}$$

where $\sigma_{\rm inv}$ is the inverse reaction cross section, S_i denotes the spin of the ith particle, p_{ij} is the CM momentum of particles i and j, and σ is the corresponding resonance production cross section. Particles 1 and 2 are those before collision, whereas particles 3 and 4 are those after collision. The resonance production cross sections subtracted from the inelastic cross section leave the string production cross sections. This becomes significant above 4.5, 3, and 2 GeV for baryon-baryon, baryon-meson, and meson-meson combinations, respectively. PYTHIA [54] was used to simulate the decay of strings into particles. The time, distance, energy, and momentum of collisions were calculated in the CM frame of the colliding particles. The produced resonances underwent decay during propagation. The partial decay widths of all possible decay channels were calculated, and one of the channels was sampled randomly. Both decays and collisions were Pauli-blocked if the phase space of the final state was occupied. To calculate the blocking probability, the phase-space occupation factor at the final states of the reaction products was calculated by Eq. (19),

$$\begin{aligned} p_{i,j} &= [1 - f(\mathbf{r_i}, \mathbf{p_i})][1 - f(\mathbf{r_j}, \mathbf{p_j})], \\ f(\mathbf{r_k}, \mathbf{p_k}) &= \sum_{l\neq k} 8\exp\left(-\frac{(\mathbf{r_k}-\mathbf{r_l})^2}{2L} - \frac{2L(\mathbf{p_k}-\mathbf{p_l})^2}{\hbar^2}\right), \end{aligned} \tag{19}$$

where $p_{i,j}$ is the probability that the reaction is not Pauli-blocked, i and j are the particle ID numbers, $\vec{r_n}$ is the spatial coordinate of the nth particle, $\vec{p_n}$ is the momentum of the nth particle, and L is the width of the wave packet (2 fm^2). In the second equation, summation was calculated over the particles with the same isospin.

C. Finalization

After 100 fm/c of time evolution all resonances decayed, and neighboring nucleons were bound to each other to form clusters. The nucleon pairs that satisfied the following conditions were bound:

(i) the distance in their CM frame was less than 4 fm, and
(ii) the difference in momentum was less than the local Fermi momentum calculated as

$$p_F = \left(\frac{3\pi^2}{2}\frac{\rho_1+\rho_2}{2}\right)^{1/3}\hbar c, \tag{20}$$

where ρ_1 and ρ_2 are the nucleon density at the nucleon positions. Binding of particles other than nucleons (i.e., formation of hypernuclei) was not considered.

Translational motion of the clusters was calculated by summing the momentum of the bound nucleons. The internal energy was obtained by summing the kinetic energy of nucleons in the nucleus rest frame. The binding energy of the nucleus was calculated based on its isotopic identity. The excitation energy of the nucleus $E_{\rm ex}$ was obtained by the equation

$$E_{\rm ex} = \sum_i \left(\sqrt{p_i^2 + m_i^2 + 2m_i^2\langle\hat{V}_i\rangle_i} - m_i\right) + E_{\rm bin}, \tag{21}$$

where $E_{\rm bin}$ denotes the binding energy of the nucleus in the ground state. If clusters with mass numbers lower than 5 had an excitation energy lower than their particle separation energies, the excitation energy was assumed to be 0 because such clusters do not have bound excitation states. When clusters with excitation energies lower than [$-0.2\times$ mass number (MeV)] were produced, the reaction event was rejected and the simulation was run afresh with the same impact parameter. If the excitation energy of a cluster was negative but higher than [$-0.2\times$ mass number (MeV)], its excitation energies were overwritten by 0.

After clusterization, the sum of the rest mass (in the case of clusters, the excitation energy was excluded), and the kinetic energy of all particles ($E_{\rm end}$) were calculated and compared with those at the beginning of the reaction ($E_{\rm ini}$). The sum of the excitation energies of all clusters at the end of the reaction ($E_{\rm ex\text{-}s}$) was calculated as well. If $E_{\rm end}$ was lower than $E_{\rm ini}$ or equal to $E_{\rm ini}$, the excitation energies of all clusters were scaled up by $(E_{\rm ini} - E_{\rm end})/E_{\rm ex\text{-}s}$ to satisfy energy conservation. If $E_{\rm end}$ was higher than $E_{\rm ini}$, the reaction simulation was rejected and started afresh by conserving the impact parameter, except for the reactions that satisfied either of the following conditions:

(i) the number of particles in the final state is more than 100, and
(ii) $\sqrt{s} -$ (rest mass) is larger than 200 GeV.

Because the local potential calculated in the previous time step was used to calculate the motion in the next time step and the equation of motion was derived using approximations, error was accumulated in every time step. Therefore the total energy fluctuated and deviated from the initial energy. This trend was particularly significant for energetic collisions, in which numerous particles were generated and interacted with each other. Therefore, in the case where the above two conditions were satisfied and the total energy exceeded the initial energy at the end of reaction, the momenta of all particles were gradually scaled down in the CM frame (typically around 0.01%) until energy conservation was satisfied. Otherwise, the reaction simulation was run afresh after conserving the impact parameter. Alternatively, if the projectile and target did not lose any nucleons after clusterization and their excitation energies were lower than their hadronic evaporation thresholds, the event was rejected because it was not an inelastic reaction event. The reaction simulation was started afresh by sampling a new impact parameter.

The residual nuclei that had excitation energy after clusterization were deexcited using the generalized evaporation model (GEM) [55]. The default version of the GEM had a shell correction, in which the shell energy correction was calculated as the sum of the proton shell correction and neutron shell correction [56]. In this study, the isotopic shell energy correction, given as the KTUY tabulation [57], was used to reproduce isotopic yields more accurately.

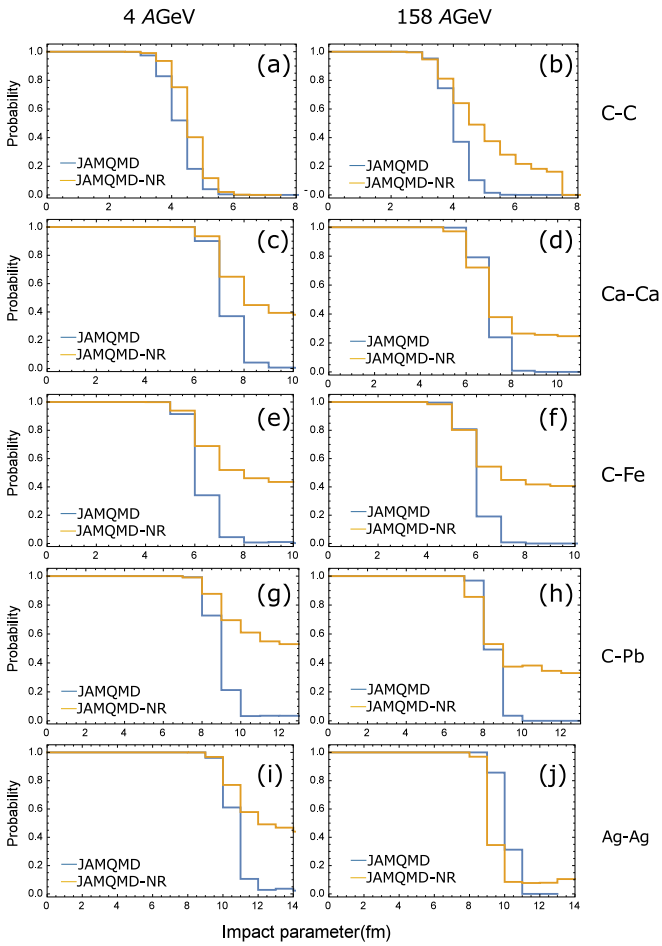

FIG. 2. Impact parameter dependence of the inelastic reaction probability.

III. RESULTS AND DISCUSSION

A. Stability of ground states and verification of total reaction cross sections

To confirm the stability of nuclei and obtain the range of impact parameters within which inelastic reactions occurred, the inelastic reaction probability was calculated by running the nucleus-nucleus collision simulation by sweeping the impact parameter from 0. The examined target-projectile combinations were ^{12}C-^{12}C, ^{40}Ca-^{40}Ca, ^{12}C-^{56}Fe, ^{12}C-^{208}Pb, and ^{107}Ag-^{107}Ag. Examined projectile incident energies were 4 and 158 A GeV in the laboratory frame. Figure 2 shows the impact parameter dependence of the inelastic reaction probability. Here reactions in which more than one nucleon was removed in the final state or in which the excitation energies of either the projectile or the target exceeded the emission threshold of either proton, neutron, or alpha were defined as inelastic reactions. JAMQMD denotes calculation by the standard version of JAMQMD, whereas JAMQMD-NR denotes calculation based on JAMQMD with the nonrelativistic equation of motion.

All the plots except Fig. 2(a) show that in JAMQMD-NR, the reaction probability does not converge to 0 when the impact parameter is large. In other words, nuclei are unstable and disintegrate from 20% to 40% owing to the nonrelativistic equation of motion. Figure 2(a) shows that the nonrelativistic treatment is valid only when very few nucleons are involved in the collision, and the incident energy is low. In Fig. 2(j), the inelastic reaction probability decreases to about 10%, but this is ascribed mainly to the events in which the total energy turns negative. Such events are classified as elastic according to the scheme described in Sec. II C, but they are eventually attributed to energy conservation failure under nonrelativistic treatment. Therefore, the Lorentz-covariant equation of motion is essential to simulate nucleus-nucleus collisions universally.

Using JAMQMD, even in the heaviest combination (^{107}Ag-^{107}Ag), the reaction probability decreases to 3% at 12 fm. This fact indicates that the self-binding nature of nuclei is well described by the mean field description and the initialization of JAMQMD. Stability during time evolution and frame transformation is essential to inhibit spurious nucleus-nucleus reactions. In all cases, the impact parameter at which the inelastic reaction probability decreases to less than 100% is independent of the incident energy. This is probably because the total nucleon-nucleon reaction cross section is almost constant in this energy range. For example, the inelastic reaction probability falls to 97% between 3 and 3.5 fm in the case of ^{12}C-^{12}C reactions at 4 A GeV. It falls further, to 0%, in the 6- to 6.5-fm range and is constantly 0 beyond 6.5 fm. At 158 A GeV, the inelastic reaction probability is 95% in the 3- to 3.5-fm region and 0% in the 5.5- to 6.0-fm region. A similar trend in which the inelastic reaction probability decreases from 100% to 0% within about 2 fm is true under the other conditions.

Based on the systematics obtained from Fig. 2, inelastic reactions occur below the impact parameter $b_{\max}$, parameterized by the equation

$$b_{\max} = 1.2 \times \left(A_t^{1/3} + A_p^{1/3}\right) \quad \text{(fm)}, \tag{22}$$

where A_t is the target mass number, and A_p is the projectile mass number.

B. Residual nuclei

The charge distribution of residual nuclei produced by nucleus-nucleus collisions was calculated to benchmark JAMQMD. The charge distribution of fragments produced by bombardment of ^{197}Au with $^{\text{Nat}}$C at 10.6 A GeV and that of fragments produced by bombardment of ^{28}Si with $^{\text{Nat}}$Cu at 14.5 A GeV were calculated and they are compared with the measurements [58,59] in Figs. 3 and 4, respectively. JAMQMD-NR denotes the calculation performed using JAMQMD with the nonrelativistic equation of motion. In JAMQMD-NR, the inelastic reaction probability does not converge to 0; therefore, the impact parameter is truncated at Eq. (22).

In Fig. 3, the yield increases with an increase in product charge up to 79 by one order of magnitude owing to peripheral collisions, whereas the yield is almost constant below 70. Both trends are well reproduced by JAMQMD. The odd-even effect is slightly overemphasized but it originates from the statistical decay phase as opposed to JAMQMD. The underestimation of yield at $Z = 79$ can probably be attributed to the absence

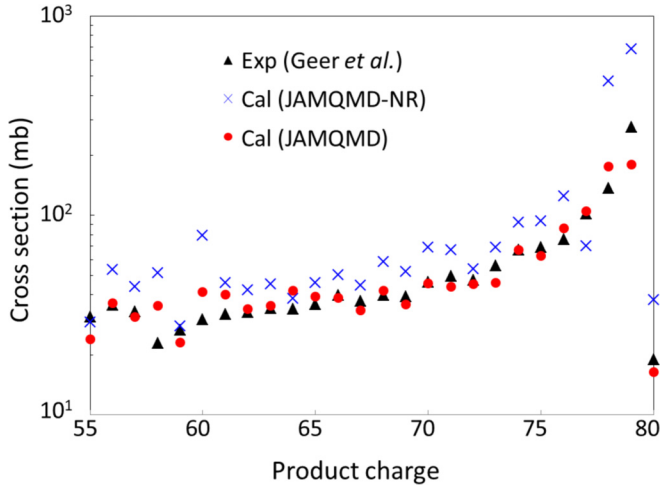

FIG. 3. Charge distribution of fragments produced in ^{197}Au($^{\mathrm{Nat}}$Cu,x) collisions at $E_{\mathrm{lab}} = 10.6$ A GeV.

of the electromagnetic dissociation mechanism. It increases the cross sections of interactions between high-Z nuclei pairs at high energy by a few 10 mb. Contrariwise, JAMQMD-NR overestimates the yield at $Z = 78$ and 79 because of spurious disintegration.

In Fig. 4, the experimental data without the contribution of electromagnetic dissociation was compared with the calculation results. In this case, the calculated cross sections agree with the measurements even at $Z = 13$. The calculation shows that the products at $Z = 12$ and 13 are about twice as abundant as the lighter products, as seen in the experimental result. It should be noted that the odd-even effect, which is shown in Fig. 4, attributed to the statistical decay phase is in good agreement between the simulation and the experiment in this case. The yield fluctuation is attributed to the q value of proton emission, which is dependent on the charge number and shell energy correction of the level density parameter. When shell energy correction data were taken from Cook *et al.* [56], the yield distribution became inaccurate (not shown). Therefore it

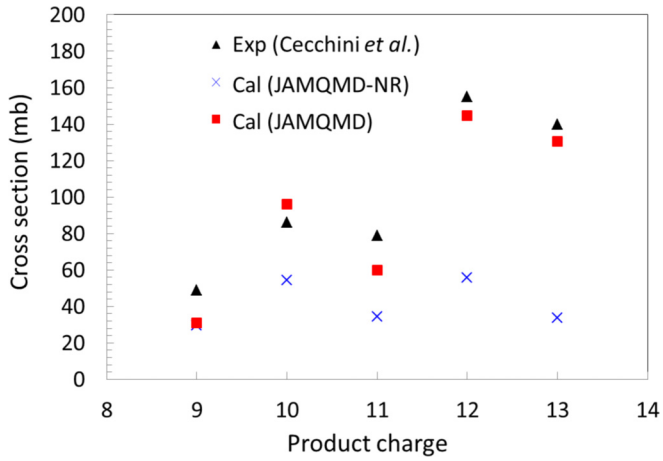

FIG. 4. Charge distribution of fragments produced in ^{28}Si($^{\mathrm{Nat}}$Cu,x) collisions at $E_{\mathrm{lab}} = 14.5$ A GeV.

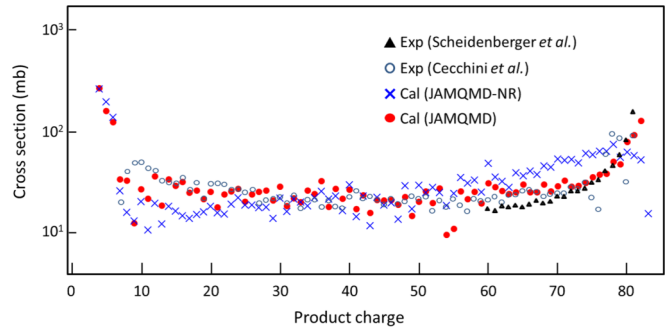

FIG. 5. Charge distribution of fragments produced in ^{208}Pb($^{\mathrm{Nat}}$C,x) collisions at $E_{\mathrm{lab}} = 158$ A GeV.

is important to use accurate shell energy correction data (the KTUY formula in this case) to reproduce the odd-even effect of the charge distribution.

JAMQMD-NR underestimates the yield at $Z = 12$ and 13 because of the impact parameter truncation. The impact parameter was cut at 8.63 fm but one- or two-nucleon knockout reactions occurred at a larger impact parameter, at which true reactions and spurious reactions could not be distinguished. The results of JAMQMD-NR in Figs. 3 and 4 indicate that the nonrelativistic version cannot predict the fragment yields regardless of the impact parameter range. Accurate treatment of the peripheral collisions by JAMQMD is crucial for simulation of fragment yields.

As an example of ultrarelativistic energy reactions, the charge distributions of fragments produced by the interaction of ^{208}Pb with $^{\mathrm{Nat}}$C and $^{\mathrm{Nat}}$Cu at 158 A GeV are shown in Figs. 5 and 6, respectively. Experimental data were taken from [60,61]. They show that production of nuclei from light to heavy is well reproduced by JAMQMD, except for reactions in which one or two nucleons are lost, which were underestimated owing to the absence of the electromagnetic dissociation mechanism. According to [60,61], the data of Scheidenberger is more reliable than those of Cecchini at high z, the fragment yield increases at high Z by a factor of 10, similarly to Fig. 3. This trend is accurately reproduced by JAMQMD, while JAMQMD-NR systematically overestimates the heavy fragments beyond $Z = 65$ in Fig. 5 and the calculated yield

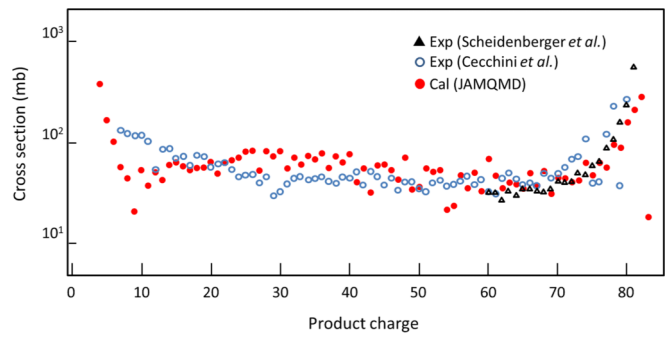

FIG. 6. Charge distribution of fragments produced in ^{208}Pb($^{\mathrm{Nat}}$Cu,x) collisions at $E_{\mathrm{lab}} = 158$ A GeV.

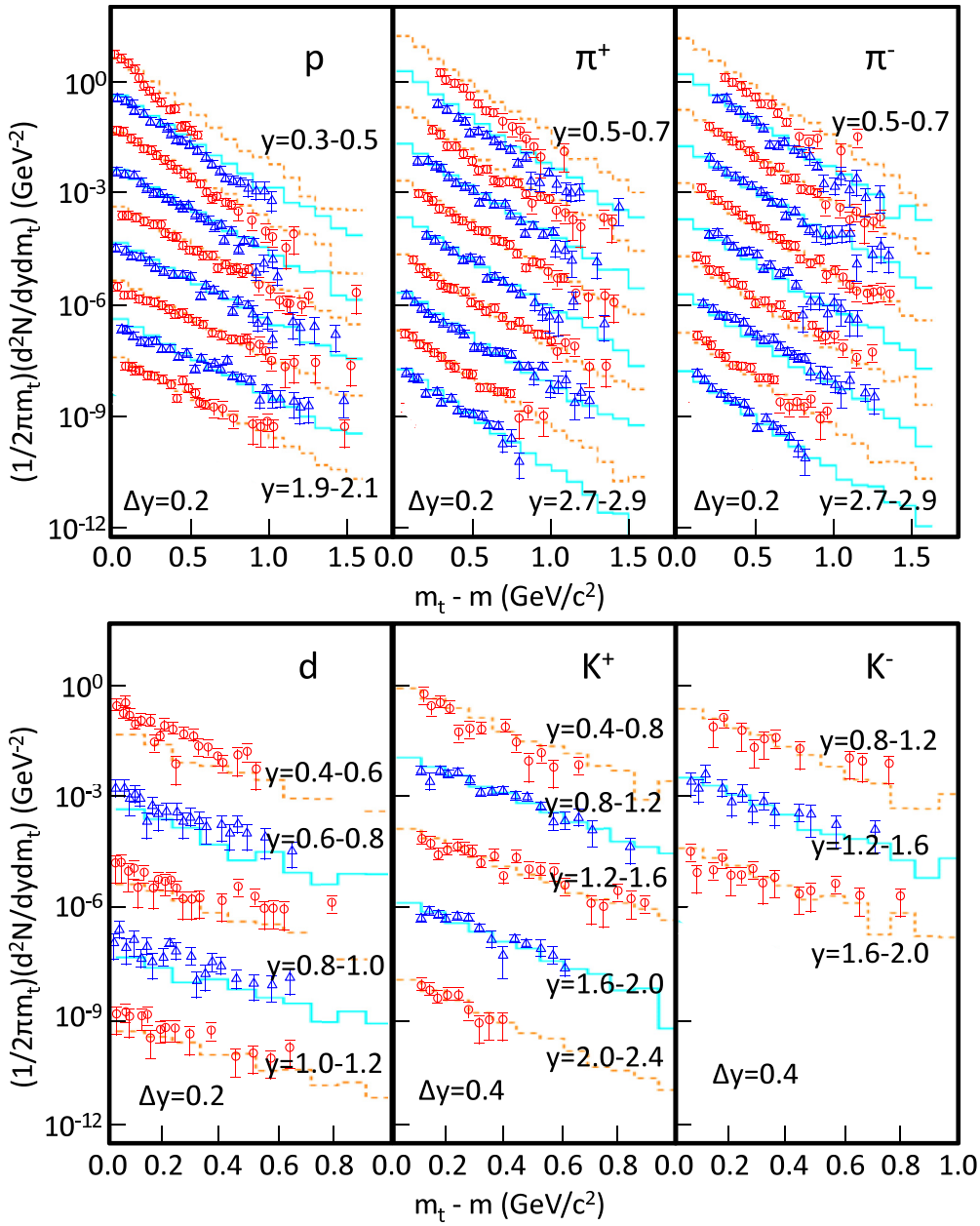

FIG. 7. Transverse mass distribution of p^+, π^-, π^+, d, K^-, and K^+ in central ^{28}Si(Al,x) collisions. The beam momentum ($p_{\rm lab}$) is 14.6 A GeV/c. Symbols and lines are experimental data and calculation by JAMQMD, respectively. For protons the rapidity is 0.3–0.5 (top spectrum) to 1.9–2.1 (bottom spectrum). The interval is 0.2. Each successive spectrum is scaled down by 10. For pions the rapidity is 0.5–0.7 (top spectrum) to 2.7–2.9 (bottom spectrum). The interval is 0.2. Each successive spectrum is scaled down by 10. For deuterons the rapidity is 0.4–0.6 (top spectrum) to 1.0–1.2 (bottom spectrum). The interval is 0.2. Each successive spectrum is scaled down by 100. For positive kaons the rapidity is 0.4–0.8 (top spectrum) to 2.0–2.4 (bottom spectrum). The interval is 0.4. Each successive spectrum is scaled down by 100. For negative kaons the rapidity is 0.8–1.2 (top spectrum) to 1.6–2.0 (bottom spectrum). The interval is 0.4. Each successive spectrum is scaled down by 100.

drops at $Z = 79$. In addition, JAMQMD-NR underestimates light fragments with charge numbers less than 20.

Reproduction of the fragment yields discussed above indicates that the following perspectives of JAMQMD are well described: initialization of nuclei, total nucleon-nucleon scattering cross sections, binding force between nucleons in the spectator part of nuclei during time evolution, and clusterization in the finalization phase. The nuclei lose a few to a few tens of nucleons in the statistical decay phase, therefore the well-reproduced general trend is attributed to the performance of JAMQMD.

C. Secondary particle production

The production of secondary particles in nucleus-nucleus collisions was benchmarked against the experimental data. The transverse mass distribution of baryons and mesons

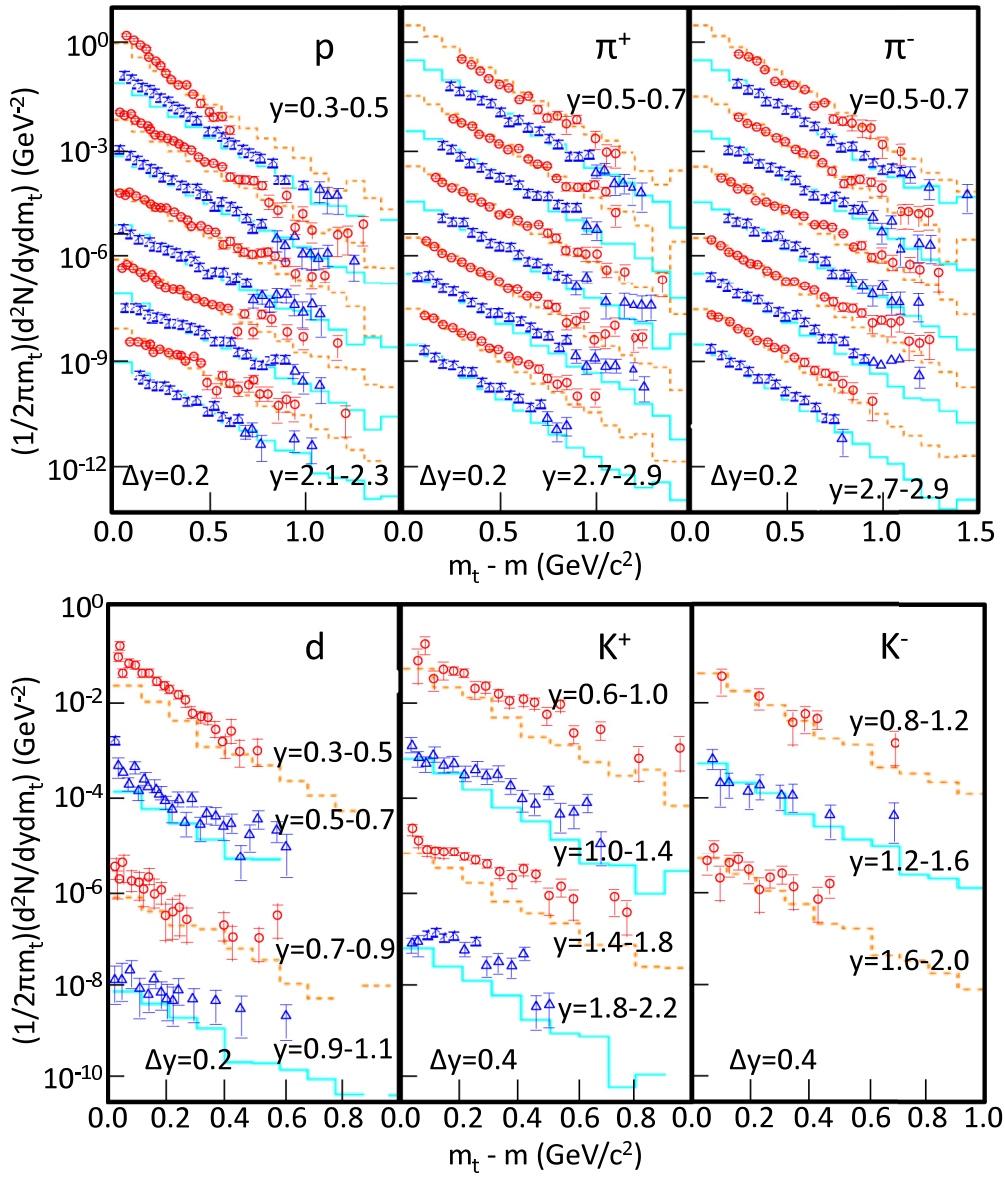

FIG. 8. Same as Fig. 7 but in peripheral ^{28}Si(Al,x) collisions. For protons the rapidity is 0.3–0.5 (top spectrum) to 2.1–2.3 (bottom spectrum). The interval is 0.2. Each successive spectrum is scaled down by 10. For pions the rapidity is 0.5–0.7 (top spectrum) to 2.7–2.9 (bottom spectrum). The interval is 0.2. Each successive spectrum is scaled down by 10. For deuterons the rapidity is 0.3–0.5 (top spectrum) to 0.9–1.1 (bottom spectrum). The interval is 0.2. Each successive spectrum is scaled down by 100. For positive kaons the rapidity is 0.6–1.0 (top spectrum) to 1.8–2.2 (bottom spectrum). The interval is 0.4. Each successive spectrum is scaled down by 100. For negative kaons the rapidity is 0.8–1.2 (top spectrum) to 1.6–2.0 (bottom spectrum). The interval is 0.4. Each successive spectrum is scaled down by 100.

in midrapidity in various nucleus-nucleus combinations was calculated. Figures 7–10 show comparisons of the transverse mass distributions of protons, π^+, π^-, K^+, K^-, and deuterons [62,63]. Events were accepted as central collisions if the particle multiplicity was greater than 62 (Al target) or 154 (Au target). If the summation of the kinetic energies of all the particles, the rest mass of short-lived particles, and the energy released by annihilation of antiparticles within 0–24.6 mrad was greater than 250 GeV, events were accepted as peripheral collisions. Pions originate from the decay of resonances or fragmentation of strings, which tend to emit particles in midrapidity. Protons, by contrast, are produced by the kick-out from projectile or target nuclei. The absolute yield and transverse mass slope are well reproduced by JAMQMD in Figs. 7–9. This indicates that the fragmentation of strings, decay of resonances, and disintegration of target and projectile nuclei are properly described by JAMQMD. In Fig. 10, JAMQMD underestimates the absolute yields of protons and pions, but the slope gradients are in good agreement.

The good agreement between calculated and measured deuteron yields is particularly important because clusterization of nucleons is one of the most unique aspects of QMD in comparison with other nucleus-nucleus collision event generators. Deuterons were produced by the default nucleon-

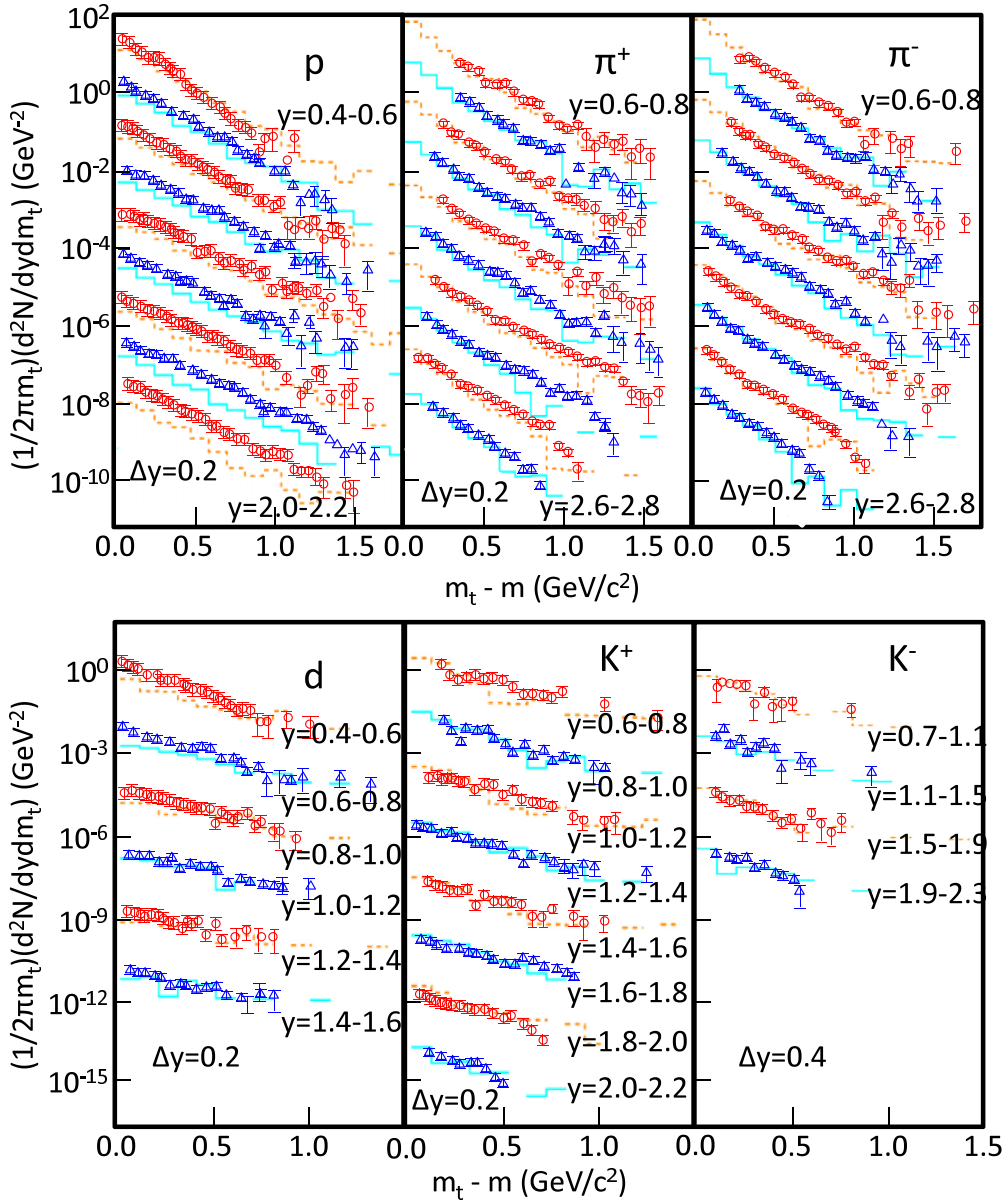

FIG. 9. Same as Fig. 7 but in central ^{28}Si(Au,x) collisions. For protons the rapidity is 0.4–0.6 (top spectrum) to 2.0–2.2 (bottom spectrum). The interval is 0.2. Each successive spectrum is scaled down by 10. For pions the rapidity is 0.6–0.8 (top spectrum) to 2.6–2.8 (bottom spectrum). The interval is 0.2. Each successive spectrum is scaled down by 10. For deuterons the rapidity is 0.4–0.6 (top spectrum) to 1.4–1.6 (bottom spectrum). The interval is 0.2. Each successive spectrum is scaled down by 100. For positive kaons the rapidity is 0.6–0.8 (top spectrum) to 2.0–2.2 (bottom spectrum). The interval is 0.2. Each successive spectrum is scaled down by 100. For negative kaons the rapidity is 0.7–1.1 (top spectrum) to 1.9–2.3 (bottom spectrum). The interval is 0.4. Each successive spectrum is scaled down by 100.

clusterization scheme based on relative distances and relative momenta as explained in Sec. II, and therefore the features of deuterons such as low binding energy were not considered. This fact suggests that midrapidity deuteron production in energetic nucleus-nucleus collisions can be well described based solely on the distances of neutron-proton pairs in the phase space.

To verify JAMQMD at higher nuclear densities, experimental data on Pb(Pb,x)X reactions at 20, 40, 80, and 158 A GeV were taken from the literature and compared with the calculation performed using JAMQMD. Figures 11–15 show comparisons of the transverse mass distribution of proton, antiproton, π^+, π^-, K^+ and K^-. In this comparison, the incident energy varies from the resonance regime to the string formation regime, but meson yields are reproduced well regardless of the incident energy. The proton yield, attributed to kick-out from the nuclei, is stably well reproduced. In contrast to the discussion on the residual nuclei in Sec. III B, the agreement of particle yields indicates reasonable treatment of the following aspects: angular distribution of the nucleon-nucleon scattering cross section, energy dependence of the resonance production cross section, mass distribution and

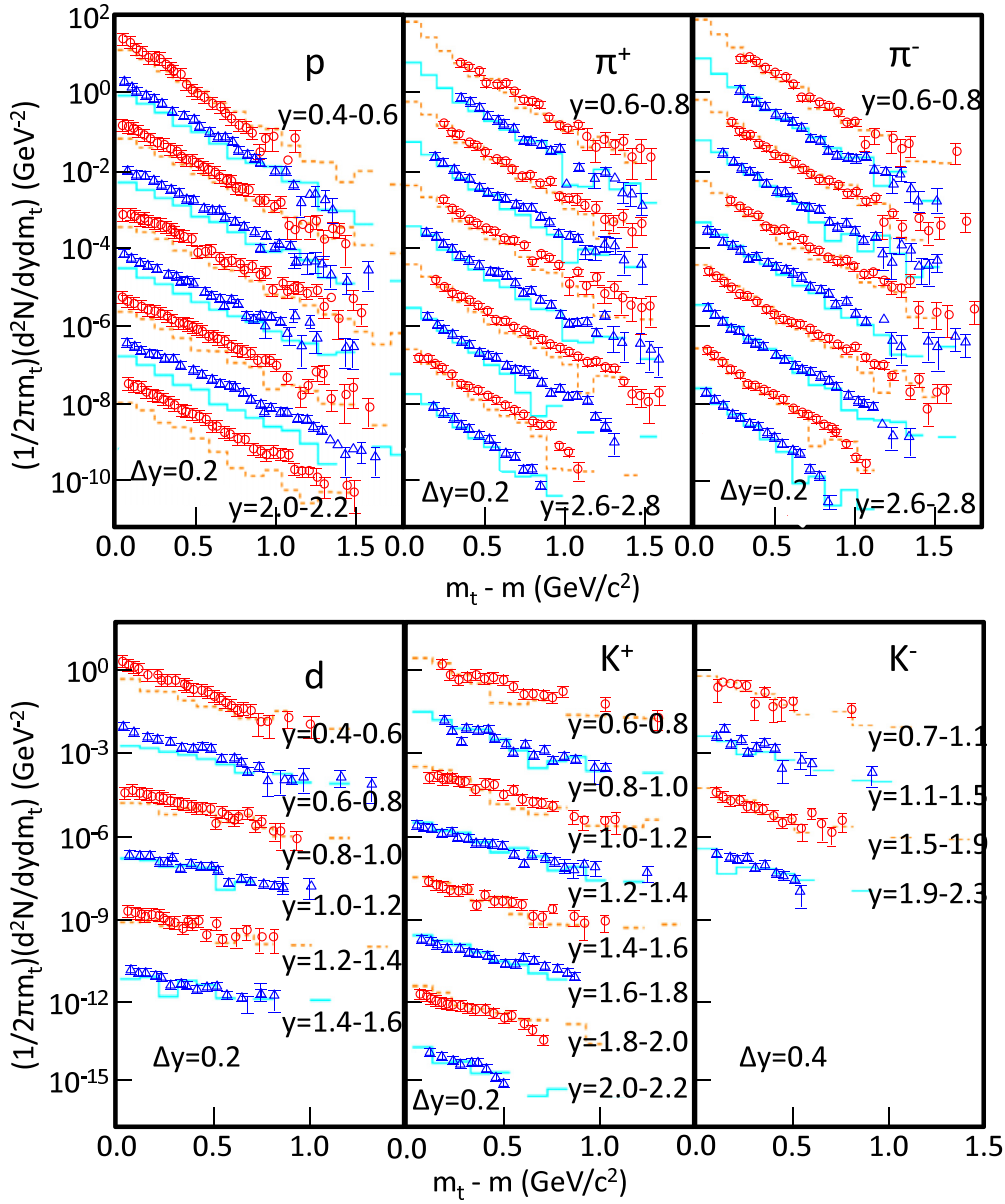

FIG. 10. The same as Fig. 7 but in peripheral ^{28}Si(Au,x) collisions. For protons the rapidity is 0.4–0.6 (top spectrum) to 2.0–2.2 (bottom spectrum). The interval is 0.2. Each successive spectrum is scaled down by 10. For pions the rapidity is 0.6–0.8 (top spectrum) to 2.6–2.8 (bottom spectrum). The interval is 0.2. Each successive spectrum is scaled down by 10. For deuterons the rapidity is 0.4–0.6 (top spectrum) to 1.0–1.2 (bottom spectrum). The interval is 0.2. Each successive spectrum is scaled down by 100. For positive kaons the rapidity is 0.7–1.1 (top spectrum) to 1.9–2.3 (bottom spectrum). The interval is 0.4. Each successive spectrum is scaled down by 100. For negative kaons the rapidity is 1.0–1.6 (top spectrum) to 1.6–2.2 (bottom spectrum). The interval is 0.6. Each successive spectrum is scaled down by 100.

decay of the resonances, string formation cross section, and fragmentation mechanism of strings. In addition, accurate deuteron production is supported by the clusterization and the mean-field interaction between proton-neutron pairs.

Figure 16 shows the comparison of the inverse slope parameter T as a function of the incident energy. The inverse slope parameter T was obtained by fitting the transverse mass distribution by an exponential decline function, $\mathrm{Exp}[-m_t/T]$. The inverse slope parameter calculated by JAMQMD was around 200 MeV and was independent of the incident energy. This trend agrees with that measured in Pb-Pb collisions, which is distinctly different from that in p + p collisions [67]. Simulation by reaction models such as URQMD [22], HSD [68], GiBUU [30], and the hydrodynamic model [69] was attempted to reproduce the inverse slope parameters. The transition to QGP is not included in all these models but the hydrodynamic model [69] succeeded in reproducing the inverse slope parameter. As JAMQMD is a hadronic reaction model based on incoherent two-body interaction, JAMQMD cannot consider the transition to QGP; but the temperature plateau probably attributable to the system volume expansion, which is not a direct consequence of QGP, was well reproduced. In

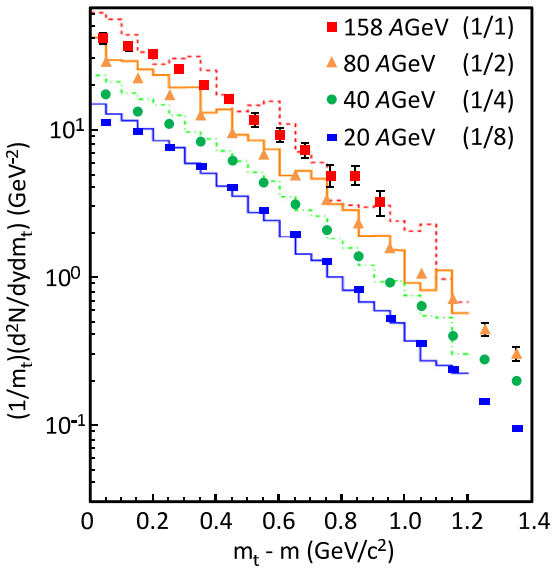

FIG. 11. Proton transverse mass distribution in central Pb-Pb collisions at 20, 40, 80, and 158 *A* GeV. Symbols are experimental data taken from [64]. Lines are result of calculations performed by JAMQMD. Each successive spectrum is scaled down by 2.

this way, JAMQMD can reproduce various nucleus-nucleus reactions unless a QGP phase transition takes effect.

IV. CONCLUSION

A quantum molecular dynamics model, JAMQMD, composed of binary reactions of elastic, resonant, and nonresonant channels, a relativistic equation of motion, interaction by mean field, and clusterization in the final state, was developed in this study. JAMQMD can reproduce various cross sections of nucleus-nucleus collisions from a few to a few hundred *A* GeV. By the relativistic equation of motion, nuclei remain stable during a typical reaction period of 100 fm/c. Otherwise,

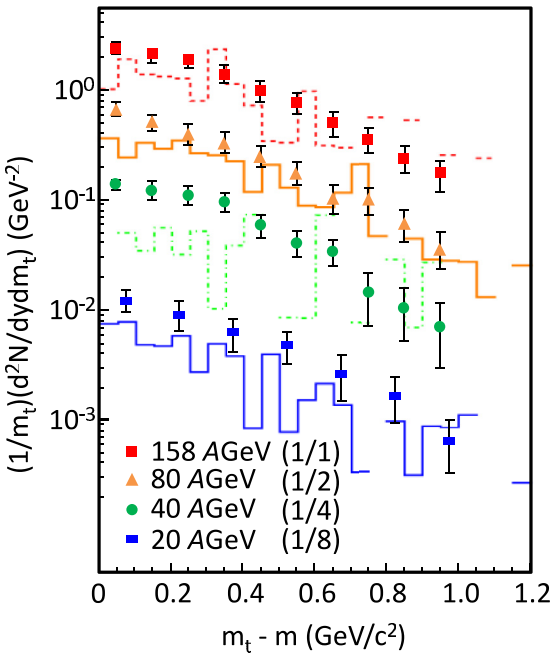

FIG. 12. Same as Fig. 11 but for antiprotons [64].

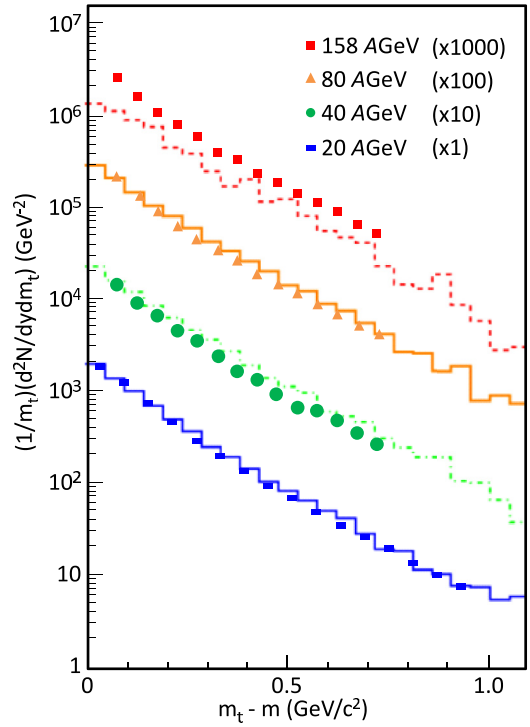

FIG. 13. Same as Fig. 11 but for π^-. Experimental data are taken from [65,66]. Each successive spectrum is scaled up by 10.

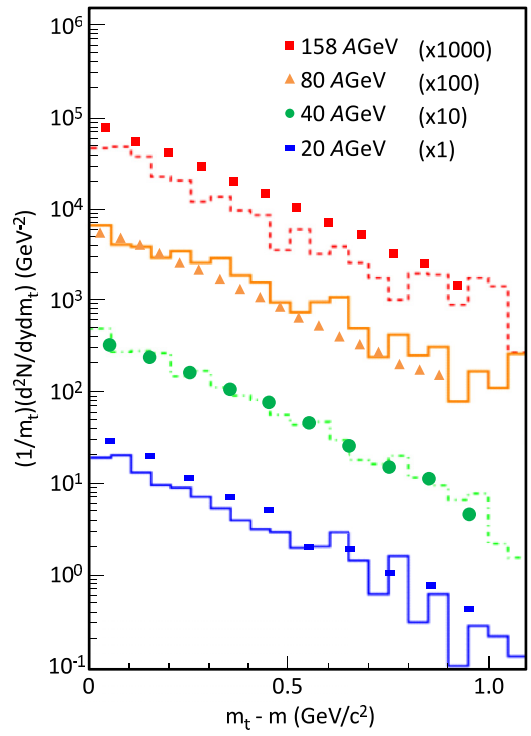

FIG. 14. Same as Fig. 11 but for K^-. Experimental data are taken from [65,66].

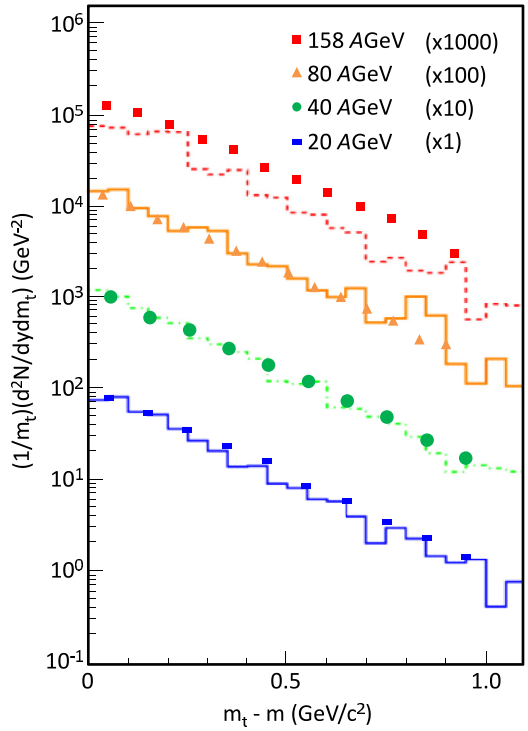

FIG. 15. Same as Fig. 11 but for K^+. Experimental data are taken from [65,66].

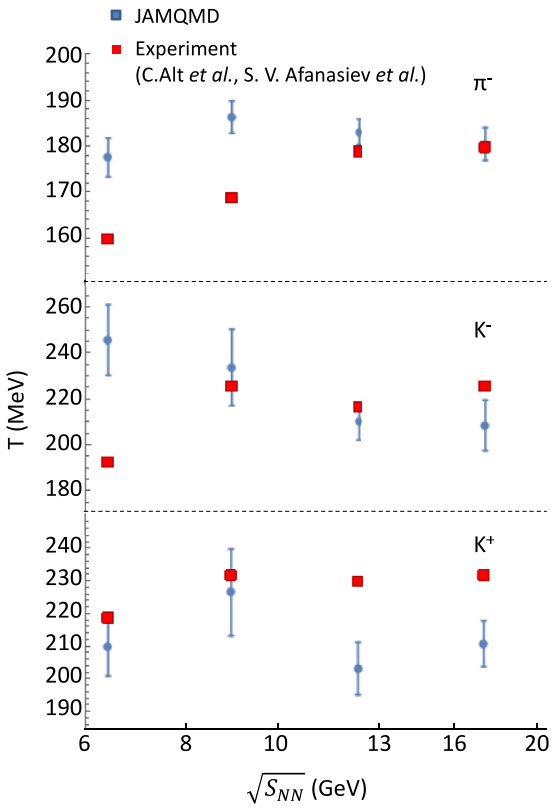

FIG. 16. Inverse slope parameters of π^-, K^-, and K^+ measured in experiments [65,66] and calculated by JAMQMD.

nuclei undergo spurious excitation or disintegration up to 40% typically.

This model, JAMQMD, was benchmarked against the measured fragment charge distribution and the measured transverse mass distribution of secondary particles in midrapidity in the energy range from a few to a few hundred A GeV. The calculated fragment mass distributions agree well with the experimental results for both light and heavy targets. The fragment mass distribution generally consists of a flat yield of light fragments attributed to deep collisions and large production cross sections for heavy fragments. The calculated results reproduced the cross sections in both regions. This indicates that JAMQMD can be used to reasonably simulate the knockout of nucleons and the binding of residues. With the nonrelativistic equation of motion, the yields of heavy fragments are underestimated or overestimated depending on the colliding nuclei; therefore, description of the equation of motion is crucial for production of large fragments attributed to peripheral collisions. The calculated transverse mass distributions of secondary particles were benchmarked against experimental data from the literature as well. Except for the absolute yields in ^{28}Si(Au,x) peripheral collisions, both the transverse mass slope and the absolute yields were well reproduced. Importantly, deuteron yields were well reproduced by the general clusterization scheme without employing any specialized mechanism such as coalescence. The good agreement of meson yields indicates reasonable formation and decay of resonance and strings. The accurate proton yield is attributed to the nucleon-nucleon scattering angle distribution.

This model will be useful for exclusive simulation of relativistic nucleus-nucleus collisions, which is important for planning heavy-ion physics experiments, and studies on galactic cosmic-ray transport. In addition to baryons and mesons, prompt gamma-ray emission can be simulated by combining JAMQMD with a statistical decay model and a gamma de-excitation model because the excitation energy and classical angular momentum of fragments are calculated on an event-by-event basis. JAMQMD can be further extended to simulate the phenomena observed in high-energy physics experiments such as the "strange horn," which appears in the $(K^+)/(\pi^+)$ ratio excitation function [66]. JAMQMD can reproduce the measured $(K^-)/(\pi^-)$ and $(K^+)/(\pi^+)$ ratios except the peak around $\sqrt{s_{NN}} = 8$ GeV; therefore, implementation of additional mechanisms responsible for the strange horn (e.g., the long-lived fireball [70] and consideration of high mass resonances [71]) is one of the best candidates for future upgrades.

ACKNOWLEDGMENTS

We wish to thank Dr. Davide Mancusi for providing the source code of R-JQMD. T.O. acknowledges Dr. T. Furuta, Dr. P. Gubler, and Dr. T. Maruyama, of the Japan Atomic Energy Agency, for useful advice on hadronic reactions at high density and high energy. We express gratitude to the operation team of the Center for Computational Science and E-systems (CCSE) at the Japan Atomic Energy Agency. Monte Carlo simulations reported in this paper were executed on a PC-cluster system of CCSE. This work was partly supported by JSPS KAKENHI Grant-in-Aid for Young Scientists B No. 26790072.

[1] G. Giuliani, H. Zheng, and A. Bonasera, The many facets of the (non-relativistic) nuclear equation of state, Prog. Part. Nucl. Phys. **76**, 116 (2014).

[2] J. Pochodzalla, The search for the liquid-gas phase transition in nuclei, Prog. Part. Nucl. Phys. **39**, 443 (1997).

[3] V. Baran, M. Colonna, V. Greco, and M. Di Toro, Reaction dynamics with exotic nuclei, Phys. Rep. **410**, 335 (2005).

[4] P. F. Michelson, W. B. Atwood, and S. Ritz, Fermi gamma-ray space telescope: High-energy results from the first year, Rep. Prog. Phys. **73**, 074901 (2010).

[5] H. Tokuno, T. Abu-Zayyad, R. Aida, M. Allen, R. Azuma, E. Barcikowski, J. W. Belz, T. Benno, D. R. Bergman, S. A. Blake *et al.*, The status of the telescope array experiment, J. Phys.: Conf. Ser. **293**, 012035 (2011).

[6] H. Flocard, S. E. Koonin, and M. S. Weiss, Three-dimensional time-dependent Hartree-Fock calculations: Application to ^{16}O + ^{16}O collisions, Phys. Rev. C **17**, 1682 (1978).

[7] K. T. R. Davies and S. E. Koonin, Skyrme-force time-dependent Hartree-Fock calculations with axial symmetry, Phys. Rev. C **23**, 2042 (1981).

[8] C. I. Pardi and P. D. Stevenson, Continuum time-dependent Hartree-Fock method for giant resonances in spherical nuclei, Phys. Rev. C **87**, 014330 (2013).

[9] K. T. R. Davies, K. R. Sandhya Devi, and M. R. Strayer, Fusion behavior in time-dependent Hartree-Fock calculations of ^{86}Kr + ^{139}La and ^{84}Kr + ^{209}Bi collisions, Phys. Rev. C **24**, 2576 (1981).

[10] K. R. Sandhya Devi, M. R. Strayer, J. M. Irvine, and K. T. R. Davies, Time-dependent Hartree-Fock collisions of ^{16}O + ^{93}Nb at $E_{\rm lab} = 204$ MeV, Phys. Rev. C **23**, 1064 (1981).

[11] S. Faidi and J. M. Irvine, TDHF studies of heavy-ion collisions leading to the compound nucleus ^{56}Ni, J. Phys. G **9**, 409 (1983).

[12] W. Bauhoff, E. Caurier, and B. Grammaticos, The time-dependent cluster model applied to the description of heavy-ion collisions, *Proceedings of the Topical Meeting on Nuclear Fluid Dynamics, Trieste, Italy, 1982*, IAEA Rep. No.: IAEA-SMR–108 (International Atomic Energy Agency (IAEA), 1983), pp. 167–172.

[13] B. G. Giraud, An introduction to the time-dependent Hartree-Fock theory in nuclear physics, in *Bifurcation Phenomena in Mathematical Physics and Related Topics* (Springer-Verlag, Berlin, 1980), pp. 555–583.

[14] J. Aichelin and H. Stocker, Quantum molecular dynamics—A novel approach to *N*-body correlations in heavy-ion collisions, Phys. Lett. B **176**, 14 (1986).

[15] J. Su, F.-S. Zhang, and B.-A. Bian, Odd-even effect in heavy-ion collisions at intermediate energies, Phys. Rev. C **83**, 014608 (2011).

[16] M. Papa, T. Maruyama, and A. Bonasera, Constrained molecular dynamics approach to fermionic systems, Phys. Rev. C **64**, 024612 (2001).

[17] M. Papa, Cluster production and nuclear dynamics, J. Phys.: Conf. Ser. **863**, 012056 (2017).

[18] Y. Zhang and Z. Li, Elliptic flow and system size dependence of transition energies at intermediate energies, Phys. Rev. C **74**, 014602 (2006).

[19] Z.-Q. Feng, Momentum dependence of the symmetry potential and its influence on nuclear reactions, Phys. Rev. C **84**, 024610 (2011).

[20] X. G. Cao, G. Q. Zhang, X. Z. Cai, Y. G. Ma, W. Guo, J. G. Chen, W. D. Tian, D. Q. Fang, and H. W. Wang, Roles of deformation and orientation in heavy-ion collisions induced by light deformed nuclei at intermediate energy, Phys. Rev. C **81**, 061603 (2010).

[21] Q. Li, Z. Li, S. Soff, M. Bleicher, and H. Stöcker, Probing the density dependence of the symmetry potential at low and high densities, Phys. Rev. C **72**, 034613 (2005).

[22] S. A. Bass, M. Belkacem, M. Bleicher, M. Brandstetter, L. Bravina, C. Ernst, L. Gerland, M. Hofmann, S. Hofmann, J. Konopka, G. Mao, L. Neise, S. Soff, C. Spieles, H. Weber, L. A. Winckelmann, H. Stocker, W. Greiner, Ch. Hartnack, J. Aichelin, and N. Amelin, Microscopic models for ultrarelativistic heavy ion collisions, Prog. Part. Nucl. Phys. **41**, 255 (1998).

[23] K. Niita, S. Chiba, T. Maruyama, T. Maruyama, H. Takada, T. Fukahori, Y. Nakahara, and A. Iwamoto, Analysis of the (N, xN') reactions by quantum molecular dynamics plus statistical decay model, Phys. Rev. C **52**, 2620 (1995).

[24] Y. Nara, N. Otuka, A. Ohnishi, K. Niita, and S. Chiba, Relativistic nuclear collisions at 10A GeV energies from p + Be to Au + Au with the hadronic cascade model, Phys. Rev. C **61**, 024901 (1999).

[25] N. Ikeno, A. Ono, Y. Nara, and A. Ohnishi, Probing neutron-proton dynamics by pions, Phys. Rev. C **93**, 044612 (2016).

[26] S. Leray, D. Mancusi, P. Kaitaniemi, J. C. David, A. Boudard, B. Braunn, and J. Cugnon, Extension of the Liege intra nuclear cascade model to light ion-induced collisions for medical and space applications, J. Phys.: Conf. Ser. **420**, 012065 (2013).

[27] K. K. Gudima, S. G. Mashnik, and A. J. Sierk, User Manual for the Code LAQGSM, Los Alamos National Laboratory Report LA-UR(01):6804 (Los Alamos National Laboratory, Los Alamos, NM, 2001).

[28] S. G. Mashnik, A. J. Sierk, K. K. Gudima, and M. I. Baznat, CEM03 and LAQGSM03—New modeling tools for nuclear applications, J. Phys.: Conf. Ser. **41**, 340 (2006).

[29] J. M. Torres-Rincon, *Boltzmann-Uehling-Uhlenbeck Equation* (Springer International, Cham, Switzerland, 2014).

[30] T. Gaitanos, A. B. Larionov, H. Lenske, and U. Mosel, Breathing mode in an improved transport approach, Phys. Rev. C **81**, 054316 (2010).

[31] S. Mallik, S. Das Gupta, and G. Chaudhuri, Event simulations in a transport model for intermediate energy heavy-ion collisions: Applications to multiplicity distributions, Phys. Rev. C **91**, 034616 (2015).

[32] B.-A. Li, L.-W. Chen, and C. M. Ko, Recent progress and new challenges in isospin physics with heavy-ion reactions, Phys. Rep. **464**, 113 (2008).

[33] P. Danielewicz, Determination of the mean-field momentum-dependence using elliptic flow, Nucl. Phys. A **673**, 375 (2000).

[34] T. Song and C. M. Ko, Modifications of the pion-production threshold in the nuclear medium in heavy-ion collisions and the nuclear symmetry energy, Phys. Rev. C **91**, 014901 (2015).

[35] J. Weil, V. Steinberg, J. Staudenmaier, L. G. Pang, D. Oliinychenko, J. Mohs, M. Kretz, T. Kehrenberg, A. Goldschmidt, B. Bäuchle, J. Auvinen, M. Attems, and H. Petersen, Particle production and equilibrium properties within a new hadron transport approach for heavy-ion collisions, Phys. Rev. C **94**, 054905 (2016).

[36] M. Colonna, Fluctuations and Symmetry Energy in Nuclear Fragmentation Dynamics, Phys. Rev. Lett. **110**, 042701 (2013).

[37] S. Roesler, R. Engel, and J. Ranft, *The Monte Carlo event generator DPMJET-III, in Advanced Monte Carlo for Radiation Physics, Particle Transport Simulation and Applications*, edited

by A. Kling, F. J. C. Barao, M. Nakagawa, L. Tavora, and P. Vaz (Springer-Verlag, Berlin, 2001), pp. 1033–1038.
[38] R. Engel and J. Ranft, Hadronic photon-photon interactions at high energies, Phys. Rev. D **54**, 4244 (1996).
[39] T. Sjostrand and M. Bengtsson, The Lund Monte Carlo for jet fragmentation and $e+$ $e-$ physics—Jetset version 6.3—An update, Comput. Phys. Commun. **43**, 367 (1987).
[40] M. D. Cozma, Y. Leifels, W. Trautmann, Q. Li, and P. Russotto, Toward a model-independent constraint of the high-density dependence of the symmetry energy, Phys. Rev. C **88**, 044912 (2013).
[41] N. Wang, Z. Li, and X. Wu, Improved quantum molecular dynamics model and its applications to fusion reaction near barrier, Phys. Rev. C **65**, 064608 (2002).
[42] H. Sorge, Flavor production in Pb(160a GeV) on Pb collisions: Effect of color ropes and hadronic rescattering, Phys. Rev. C **52**, 3291 (1995).
[43] H. Feldmeier and J. Schnack, Fermionic molecular dynamics, Prog. Part. Nucl. Phys. **39**, 393 (1997).
[44] A. Ono, H. Horiuchi, T. Maruyama, and A. Ohnishi, Fragment Formation Studied with Antisymmetrized Version of Molecular Dynamics with Two-Nucleon Collisions, Phys. Rev. Lett. **68**, 2898 (1992).
[45] A. Schwarzschild and Č. Zupančič, Production of tritons, deuterons, nucleons, and mesons by 30-GeV protons on Al, Be, and Fe targets, Phys. Rev. **129**, 854 (1963).
[46] S. T. Butler and C. A. Pearson, Deuterons from high-energy proton bombardment of matter, Phys. Rev. **129**, 836 (1963).
[47] D. Mancusi, K. Niita, T. Maruyama, and L. Sihver, Stability of nuclei in peripheral collisions in the JAERI quantum molecular dynamics model, Phys. Rev. C **79**, 014614 (2009).
[48] T. Ogawa, T. Sato, S. Hashimoto, D. Satoh, S. Tsuda, and K. Niita, Energy-dependent fragmentation cross sections of relativistic ^{12}C, Phys. Rev. C **92**, 024614 (2015).
[49] R. M. Barnett, C. D. Carone, D. E. Groom, T. G. Trippe, C. G. Wohl, B. Armstrong, P. S. Gee, G. S. Wagman, F. James, M. Mangano *et al.*, Review of particle physics, Phys. Rev. D **54**, 1 (1996).
[50] M. Kohno, M. Higashi, Y. Watanabe, and M. Kawai, In-medium nucleon-nucleon cross sections from nonrelativistic reaction matrices in nuclear matter, Phys. Rev. C **57**, 3495 (1998).
[51] K. Geiger, Parton cascade description of heavy-ion collisions at CERN, Czechoslovak J. Phys. **48**, 37 (1998).
[52] K. Goulianos, Diffractive interactions of hadrons at high energies, Phys. Rep. **101**, 169 (1983).
[53] Gy. Wolf, W. Cassing, W. Ehehalt, and U. Mosel, Eta and dilepton production in heavy-ion reactions, Prog. Part. Nucl. Phys. **30**, 273 (1993).
[54] T. Sjostrand, P. Eden, C. Friberg, L. Lonnblad, G. Miu, S. Mrenna, and E. Norrbin, High-energy-physics event generation with Pythia-6.1, Comput. Phys. Commun. **135**, 238 (2001).
[55] S. Furihata, Statistical analysis of light fragment production from medium energy proton-induced reactions, Nucl. Instrum. Methods Phys. Res. B: Beam Interact. Mate. Atoms **171**, 251 (2000).
[56] J. L. Cook, H. Ferguson, and A. R. de L Musgrove, Nuclear level densities in intermediate and heavy nuclei, Aust. J. Phys. **20**, 477 (1967).
[57] H. Koura, T. Tachibana, M. Uno, and M. Yamada, Nuclidic mass formula on a spherical basis with an improved even-odd term, Prog. Theor. Phys. **113**, 305 (2005).
[58] L. Y. Geer, J. Klarmann, B. S. Nilsen, C. J. Waddington, W. R. Binns, J. R. Cummings, and T. L. Garrard, Charge-changing fragmentation of 10.6 GeV/nucleon ^{197}Au nuclei, Phys. Rev. C **52**, 334 (1995).
[59] S. Cecchini, H. Dekhissi, G. Giacomelli, G. Mandrioli, A. R. Margiotta, L. Patrizii, F. Predieri, P. Serra, and M. Spurio, Fragmentation cross sections and search for nuclear fragments with fractional charge in relativistic heavy ion collisions, Astropart. Phys. **1**, 369 (1993).
[60] S. Cecchini, G. Giacomelli, M. Giorgini, G. Mandrioli, L. Patrizii, V. Popa, P. Serra, G. Sirri, and M. Spurio, Fragmentation cross sections of 158A GeV Pb ions in various targets measured with CR39 nuclear track detectors, Nucl. Phys. A **707**, 513 (2002).
[61] C. Scheidenberger, I. A. Pshenichnov, K. Sümmerer, A. Ventura, J. P. Bondorf, A. S. Botvina, I. N. Mishustin, D. Boutin, S. Datz, H. Geissel *et al.*, Charge-changing interactions of ultrarelativistic Pb nuclei, Phys. Rev. C **70**, 014902 (2004).
[62] T. Abbott, Y. Akiba, D. Alburger, D. Beavis, R. R. Betts, L. Birstein, M. A. Bloomer, P. D. Bond, C. Chasman, Y. Y. Chu *et al.*, Forward and transverse energies in relativistic heavy ion collisions at 14.6A GeV/c per nucleon, Phys. Rev. C **44**, 1611 (1991).
[63] T. Abbott, Y. Akiba, D. Beavis, M. A. Bloomer, P. D. Bond, C. Chasman, Z. Chen, Y. Y. Chu, B. A. Cole, J. B. Costales *et al.*, Charged hadron distributions in central and peripheral Si + A collisions at 14.6A GeV/c, Phys. Rev. C **50**, 1024 (1994).
[64] C. Alt *et al.* (NA49 Collaboration), Energy and centrality dependence of $\overline{p}$ and p production and the $\overline{\Lambda}/\overline{p}$ ratio in Pb + Pb collisions between 20*A* GeV and 158*A* GeV, Phys. Rev. C **73**, 044910 (2006).
[65] C. Alt, T. Anticic, B. Baatar, D. Barna, J. Bartke, L. Betev, H. Białkowska, C. Blume, B. Boimska, M. Botje *et al.*, Pion and kaon production in central Pb + Pb collisions at 20*A* and 30*A* GeV: Evidence for the onset of deconfinement, Phys. Rev. C **77**, 024903 (2008).
[66] S. V. Afanasiev, T. Anticic, D. Barna, J. Bartke, R. A. Barton, M. Behler, L. Betev, H. Białkowska, A. Billmeier, C. Blume *et al.*, Energy dependence of pion and kaon production in central Pb + Pb collisions, Phys. Rev. C **66**, 054902 (2002).
[67] M. Kliemant, B. Lungwitz, and M. Gaździcki, Energy dependence of transverse mass spectra of kaons produced in $p + p$ and $p + \overline{p}$ interactions: A compilation, Phys. Rev. C **69**, 044903 (2004).
[68] W. Ehehalt and W. Cassing, Relativistic transport approach for nucleus-nucleus collisions from SIS to SPS energies, Nucl. Phys. A **602**, 449 (1996).
[69] Yu. B. Ivanova and V. N. Russkikh, Transverse-mass effective temperature in heavy-ion collisions from AGS to SPS, Eur. Phys. J. A **37**, 139 (2008).
[70] B. Tomášik and E. E. Kolomeitsev, Complete strangeness measurements in heavy-ion collisions, Eur. Phys. J. A **52**, 251 (2016).
[71] A. Andronic, P. Braun-Munzinger, and J. Stachel, Thermal hadron production in relativistic nuclear collisions: The hadron mass spectrum, the horn, and the QCD phase transition, Phys. Lett. B **673**, 142 (2009).